error for the results without filtering. Filtering decreases the amount of error by more than an order of magnitude with a comparatively small increase in computational time.

It is also evident that even very coarse grids (for example, a 70×70 grid) with filtering can outperform a dense grid (for example, a 250×250 grid) without filtering. The effect of filtering appears to be more significant than for the linear cases shown. Note that the error reduces very slowly as the grid is refined. As a check, the Euler code was run with a very-small-amplitude initial disturbance. For this case, which is in the linear regime, the error drops in accord with the fourth-order accuracy of the boundary conditions. However, for the nonlinear case shown here (Fig. 4), the drop is much slower (almost zeroth order). This implies that for nonlinear waves the order of the Tam and Webb[2] boundary conditions is reduced, as expected by the far-field assumption used.

Results from the solution of nonlinear Euler equations on nonuniform meshes (not shown here) show behavior similar to those of the LEE discussed.

Conclusions

A filtering strategy for improving CAA computations is demonstrated in this Note. Benchmark cases were chosen for the one- and two-dimensional LEE and full Euler equations. The results confirm that compact finite difference schemes satisfy the stringent requirements of CAA on accuracy and dispersion and diffusion errors.

Filtering appears to be an important tool in CAA. Because it suppresses the unwanted q waves, it can be used as an alternative to grid refinement. Filtering adds only an 18% additional computational cost. It was found that, to get the same quality results without filtering, a substantial increase in CPU time is needed. We also found that it enhances the stability of the numerical method and the boundary conditions.

Finally, stretched-grid studies showed that spurious oscillations arise due to inadequate local grid resolution, as opposed to errors due to variable mesh spacing.

Acknowledgments

This work was sponsored by the NASA John H. Glenn Research Center at Lewis Field under Grant NAG3-2095. J. R. Scott served as the Technical Monitor.

References

[1]Hardin, J. C., Ristorcelli, J. R., and Tam, C. K. W. (eds.), "ICASE/LARC Workshop on Benchmark Problems in Computational Aeroacoustics," NASA CP-3300, May 1995.

[2]Tam, C. K. W., and Webb, J. C., "Dispersion-Relation-Preserving Finite Difference Schemes for Computational Aeroacoustics," *Journal of Computational Physics*, Vol. 107, Aug. 1993, pp. 262–281.

[3]Lele, S. K., "Compact Finite Difference Schemes for Computational Aeroacoustics," *Journal of Computational Physics*, Vol. 103, Jan. 1992, pp. 16–42.

[4]Thompson, K. W., "Time Dependent Boundary Conditions for Hyperbolic Systems," *Journal of Computational Physics*, Vol. 68, Jan. 1987, pp. 1–24.

[5]Giles, M. B., "Nonreflecting Boundary Conditions for Euler Equation Calculations," *AIAA Journal*, Vol. 28, No. 12, 1990, pp. 2050–2058.

[6]Tam, C. K. W., "Advances in Numerical Boundary Conditions for Computational Aeroacoustics," AIAA Paper 97-1774, Jan. 1997.

[7]Spyropoulos, E. T., and Blaisdell, G. A., "Evaluation of the Dynamics Model for Simulations of Compressible Decaying Isotropic Turbulence," *AIAA Journal*, Vol. 34, No. 5, 1996, pp. 990–998.

[8]Visbal, M. R., and Gaitonde, D. V., "High Order Accurate Methods for Unsteady Vortical Flows on Curvilinear Meshes," AIAA Paper 98-0131, Jan. 1998.

[9]Hu, F. Q., "Application of PML Absorbing Boundary Conditions to Benchmark Problems of Computational Aeroacoustics," *Proceedings of the Second Computational Aeroacoustics (CAA) Workshop on Benchmark Problems*, NASA CP-3352, 1996, pp. 119–151.

[10]Koutsavdis, E. K., Blaisdell, G. A., and Lyrintzis, A. S., "On the Use of Compact Schemes with Spatial Filtering in Computational Aeroacoustics," AIAA Paper 99-0360, Jan. 1999.

[11]Vichnevetsky, R., "Invariance Theorems Concerning Reflection at Numerical Boundaries," *Journal of Computational Physics*, Vol. 63, No. 2, 1986, pp. 268–282.

P. J. Morris
Associate Editor

Drag Reduction with a Sliding Wall in Flow over a Circular Cylinder

Byunggwi Choi* and Haecheon Choi†
Seoul National University,
Seoul 151-742, Republic of Korea

Introduction

A NEW idea for reducing skin-friction drag by introducing a passively moving (sliding) belt that replaces the rigid wall in a turbulent boundary layer was presented by Bechert et al.[1] Their basic idea is to release the no-slip condition by implementing a moving wall that is driven by the flow shear stress itself. Thus, the control device does not require any input power, and it is a purely passive device. They implemented a sliding belt in their oil channel. The sliding belt reduced the velocity difference between the mean flow and the wall and reduced the skin friction by 9%. It was shown that the measured belt velocity varied between 6 and 12% of the centerline velocity, depending on the belt tension. Issues related to the implementation of the sliding belt are addressed in detail by Bechert et al.[1]

An idea similar to that of Bechert et al.[1] may be applied to bluff-body problems such as flow over a circular cylinder to reduce the form drag. That is, implementing the moving wall, which is passively driven by the wall shear stress, on a part of the cylinder surface increases the momentum nearby. The increased momentum near the wall may be large enough to overcome the adverse pressure gradient formed at the rear part of the cylinder and to delay the separation, resulting in the form-drag reduction. This concept is tested in the present study by numerical simulations.

Sliding Wall

Figure 1 shows a schematic of the sliding-belt device installed in a circular cylinder to realize the sliding-wall concept. The belts are located on the upper and lower parts of the cylinder surface. Here θ' and γ denote the front location and length of the sliding belt, respectively. The total shear force exerted on the lower sliding belt is

$$F = (1 - \mu_s) \int_A \tau \, \mathrm{d}A = ma \tag{1}$$

where m is the mass of the belt, a the acceleration, τ the flow shear stress, μ_s the friction coefficient between the belt and pulley, and A the area of the belt surface. The flow shear stress τ on the belt is written in cylindrical coordinates (r, θ) as

$$\tau = \mu \left(\frac{\partial u_\theta}{\partial r} - \frac{u_\theta}{R} \right)_{r=R} \tag{2}$$

where u_θ is the velocity in the azimuthal direction, R is the radius of the cylinder, and μ is the viscosity.

From Eqs. (1) and (2), the acceleration of the lower belt can be obtained as

$$a = \frac{\mathrm{d}u_w}{\mathrm{d}t} = \alpha \left(R \overline{\left. \frac{\partial u_\theta}{\partial r} \right|_{r=R}} - u_w \right) \tag{3}$$

where u_w is the belt (sliding-wall) velocity, $\alpha = (1 - \mu_s)\mu A / mR$, and an overbar denotes the spatial averaging over the lower sliding belt. Note that $u_w = \bar{u}_\theta|_{r=R}$ for the lower belt and $u_w = -\bar{u}_\theta|_{r=R}$ for the upper belt (Fig. 1). Equation (3) is numerically integrated in time to obtain the time sequence of the lower-belt velocity. The velocity of the upper belt can be similarly obtained.

Received 8 March 1999; revision received 19 October 1999; accepted for publication 2 November 1999.

*Graduate Student, School of Mechanical and Aerospace Engineering.

†Associate Professor, School of Mechanical and Aerospace Engineering; choi@socrates.snu.ac.kr. Member AIAA.

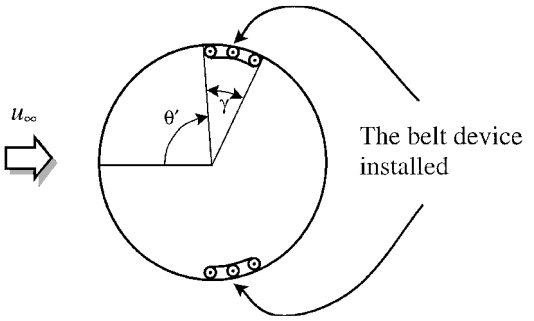

Fig. 1 Schematic of the sliding-belt device on a circular cylinder.

Numerical Method

In this study, we numerically simulate the unsteady incompressible Navier–Stokes and continuity equations. A fully implicit (Crank–Nicolson) fractional step method is used in time, and a second-order central difference method is used in space with a staggered mesh.[2] The computational domain used is $-50d < x < 20d$ and $-50d < y < 50d$, where x and $y = 0$ correspond to the center location of the cylinder in the Cartesian coordinate system and d is the cylinder diameter. A C-type grid system is used, where a nonuniform mesh of 321×121 points is created using a hyperbolic grid generation technique, and 64 grid points are located on the cylinder surface. A convective outflow condition is used for the outflow boundary condition, and Dirichlet boundary conditions are used at far-field boundaries. No-slip conditions are applied to the cylinder surface except for the sliding wall.

The Reynolds number investigated in this study is 100 based on the freestream velocity u_∞ and the cylinder diameter d. For all of the cases investigated, we have used a computational time step $\Delta t = 0.06d/u_\infty$, which corresponds to a maximum Courant–Friedrichs–Lewy number (CFL) $\simeq 4$. The present grid system, computational domain, boundary conditions, and computational time step have been substantially tested in this study (see also Kwon and Choi[3] and Park et al.[4]). The predicted Strouhal number at $Re = 100$ was 0.165, which is in excellent agreement with those obtained by Williamson[5] and Henderson.[6] We have also doubled the number of grid points (128 grid points on the cylinder surface) to check the numerical resolution in the presence of sliding walls ($\gamma = 22.5$ deg, $\theta' = 45$ and 67.5 deg) and found that the wall pressure distribution was little changed by doubling the number of grid points and that the total and form drags were changed by less than 0.5%.

Results

For a given fluid, a large α in Eq. (3) corresponds to the case of a belt of small m or small μ_s. Thus, the belt quickly reacts to the wall shear stress exerted on its surface at a large α, whereas the belt slowly reacts to the wall shear stress at a small α. Therefore, we investigate the variation of the belt velocity with respect to α for the case of $\gamma = 22.5$ deg and $\theta' = 67.5$ deg. Figure 2 shows the variations of the upper and lower belt velocities with respect to α. As α becomes larger, the belt reaches a terminal velocity more quickly. For large α ($\alpha = 1.65$ and 0.165), the terminal velocities are nearly the same, indicating that there exists a maximum terminal velocity for given γ and θ'. The terminal velocity becomes smaller at a smaller α. A phase difference between the velocities of the upper and lower belts is caused by vortex shedding behind the cylinder, and oscillations of the belt velocity become fewer at a smaller α. Therefore, the drag-reduction performance of the sliding belt depends on the magnitude of α, and the amount of drag reduction becomes less at a smaller α (not shown in this Note). However, the exact value of α cannot be determined from a purely numerical study, and thus, we consider only an ideal case of $\alpha = 0.165$ from now on, in which the belt quickly reacts to the wall shear stress as shown in Fig. 2 because our goal is to investigate a possibility of the form-drag reduction by the sliding wall.

Figure 3 shows the variation of the belt velocity with respect to the belt location θ'. We have considered four cases ($\theta' = 45$, 67.5, 90, and 112.5 deg) with $\gamma = 22.5$ deg. For the case of $\theta' = 112.5$ deg, a part of the belt locates inside the recirculation zone. (The separation point without the belt is 118 deg from the stagnation point at $Re = 100$, and the belt is located at 112.5 ~ 135 deg.) The terminal velocity becomes larger when the belt is installed closer to the stagnation point, that is, smaller θ', and it is negative when the belt is located inside the recirculation zone.

Figure 4 shows the variations of the total drag, skin-friction drag, and form drag with respect to θ'. Sliding belts of $\gamma = 22.5$ deg start to move at $tu_\infty/d = 0$. The maximum total-drag reduction of about 11% is obtained with the belt of $\theta' = 67.5$ deg, and drag increases with $\theta' = 112.5$ deg. Except for $\theta' = 112.5$ deg, the skin-friction and form drags are smaller than those with no belt. The skin-friction drag monotonically decreases as θ' decreases from 90 to 45 deg, whereas

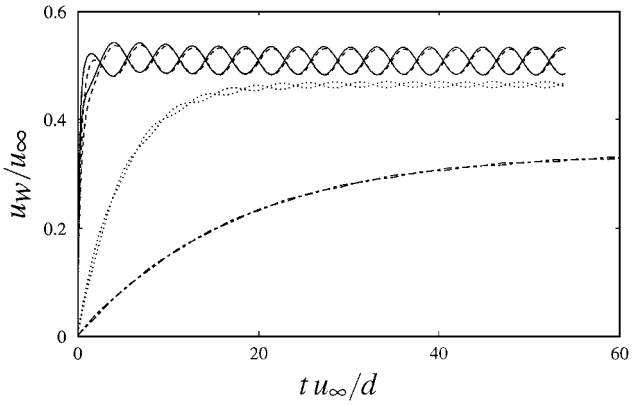

Fig. 2 Variations of the upper and lower belt velocities u_w with respect to α ($\gamma = 22.5$ deg and $\theta' = 67.5$ deg): ——, $\alpha = 1.65$; - - - -, $\alpha = 0.165$; · · ·, $\alpha = 0.00825$; and – – –, $\alpha = 0.00165$.

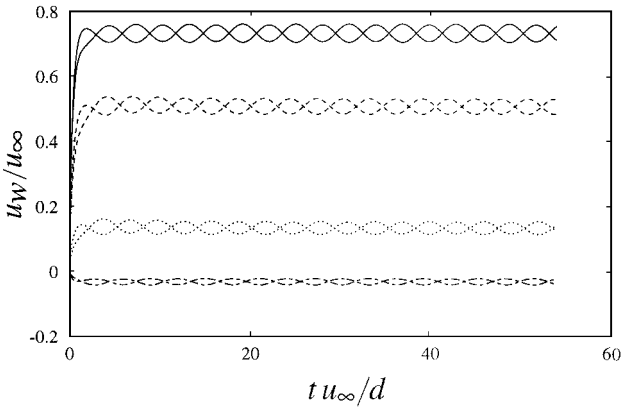

Fig. 3 Variation of the belt velocity with respect to the belt location θ' ($\gamma = 22.5$ deg): ——, $\theta' = 45$; - - - -, $\theta' = 67.5$; · · ·, $\theta' = 90$; and – – –, $\theta' = 112.5$ deg.

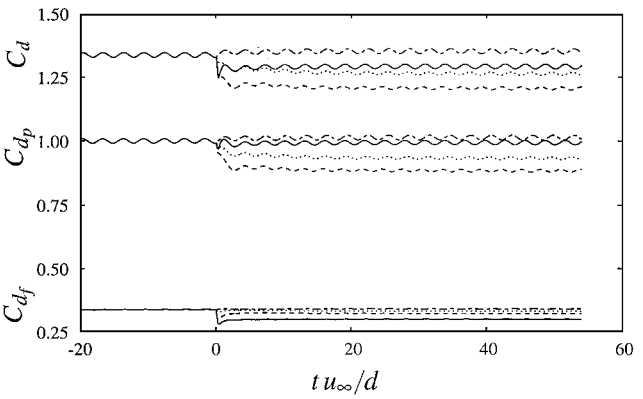

Fig. 4 Variations of the total drag C_d, form drag C_{dp}, and skin-friction drag C_{df} coefficients ($\gamma = 22.5$ deg): ——, $\theta' = 45$; - - - -, $\theta' = 67.5$; · · ·, $\theta' = 90$; and – – –, $\theta' = 112.5$ deg; solid lines at $t < 0$ correspond to the case of no belt.

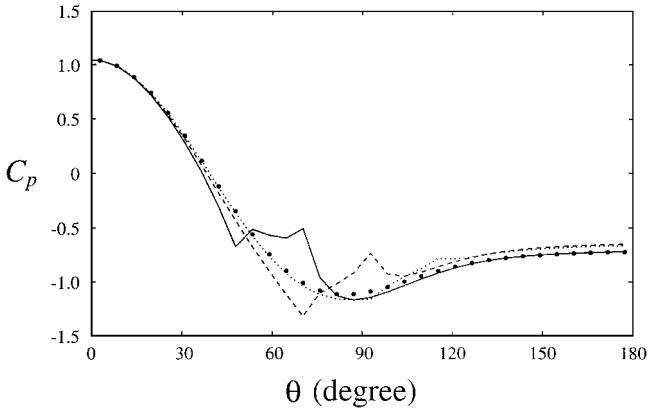

Fig. 5 Time-averaged pressure coefficients at the cylinder surface (γ = 22.5 deg): ●, no belt; ——, θ' = 45; - - - -, θ' = 67.5; and · · · ·, θ' = 90 deg.

the form drag shows a nonmonotonic behavior, that is, the reduction is maximum at $\theta' = 67.5$ deg. The decrease in the form drag is associated with the delay of the separation point (118, 123, 126, and 114 deg, respectively, for the cases of $\theta' = 45$, 67.5, 90, and 112.5 deg) through the addition of near-wall momentum by the sliding belt and also with the reduced pressure on the front surface of the cylinder. The form drag increase with $\theta' = 112.5$ deg is due to the early separation. Figure 5 shows that the surface pressure at $\theta = 50 \sim 70$ deg is significantly reduced in the case of $\theta' = 67.5$ deg, as compared to other cases. Also, the increase in the base pressure due to the separation delay is notable for the cases of $\theta' = 67.5$ and 90 deg. In the case of $\theta' = 67.5$ deg, about 5% of form drag is reduced due to the reduced pressure on the front cylinder surface and 6% due to the increased pressure on the rear surface.

To see the effect of the belt length, we double the length, $\gamma = 45$ deg. The belt location is varied as $\theta' = 45$, 56, and 67.5 deg. Reductions of total drag are about 22, 28, and 27%, respectively, for the cases of $\theta' = 45$, 56, and 67.5 deg. Thus, the amount of drag reduction is about 2.5 times larger than that of $\gamma = 22.5$ deg. For the case of maximum drag reduction (28%), the terminal belt velocity is about $0.75u_\infty$.

The Strouhal number defined as $Sr = fd/u_\infty$ is $0.164 \sim 0.165$ at $Re = 100$ for the case of no belt,[3–6] where f is the frequency. In general, the Strouhal number decreases when vortex shedding behind a cylinder is controlled to produce drag reduction by a control device such as a splitter plate attached to the cylinder (see Kwon and Choi[3] and the references therein). However, the sliding belt increases the velocity near the wall, and thus, the interaction period of the vortices generated from upper and lower surfaces becomes shorter. Therefore, the Strouhal number increases with the belt even though drag reduction occurs. For example, $Sr = 0.172$ for the case of $\gamma = 22.5$ deg and $\theta' = 67.5$ deg and $Sr = 0.181$ for the case of $\gamma = 45$ deg and $\theta' = 56$ deg.

So far, we have dealt with a very ideal case. When the belt device is implemented in a real situation, the belt velocity and the amount of drag reduction should be less than those obtained from the present study due to various losses existing in the belt device.[1] Because we cannot exactly implement the real situation in our simulation, we simply assume that because of various losses the terminal velocity of the belt is reduced to a certain value such as $u_w = 0.2$, 0.4, $0.6u_\infty$ for the case of $\gamma = 45$ deg and $\theta' = 56$ deg ($u_w \simeq 0.75u_\infty$ for the ideal case) and investigate how the drag-reduction performance of the belt device is affected in these cases. It turns out that the amount of total-drag reduction is linearly proportional to the magnitude of the terminal belt velocity and nonnegligible drag reductions are obtained: drag reductions of about 8, 15, and 22% for $u_w = 0.2$, 0.4, and $0.6u_\infty$, respectively.

Conclusion

In conclusion, the present study shows that the concept of the passively moving wall for skin-friction reduction introduced by Bechert et al.[1] is also valid for the reduction of the form drag generated from a bluff-body flow.

Acknowledgment

This work is sponsored by the Creative Research Initiatives through the Korean Ministry of Science and Technology.

References

[1]Bechert, D. W., Hage, W., and Brusek, M., "Drag Reduction with the Slip Wall," *AIAA Journal*, Vol. 34, No. 5, 1996, pp. 1072–1074.

[2]Choi, H., and Moin, P., "Effects of the Computational Time Step on Numerical Solutions of Turbulent Flow," *Journal of Computational Physics*, Vol. 113, No. 1, 1994, pp. 1–4.

[3]Kwon, K., and Choi, H., "Control of Laminar Vortex Shedding Behind a Circular Cylinder Using Splitter Plates," *Physics of Fluids*, Vol. 8, No. 2, 1996, pp. 479–486.

[4]Park, J., Kwon, K., and Choi, H., "Numerical Solutions of Flow past a Circular Cylinder at Reynolds Numbers up to 160," *KSME International Journal*, Vol. 12, No. 6, 1998, pp. 1200–1205.

[5]Williamson, C. H. K., "Oblique and Parallel Modes of Vortex Shedding in the Wake of a Circular Cylinder at Low Reynolds Numbers," *Journal of Fluid Mechanics*, Vol. 206, 1989, pp. 579–627.

[6]Henderson, R. D., "Details of the Drag Curve near the Onset of Vortex Shedding," *Physics of Fluids*, Vol. 7, No. 9, 1995, pp. 2102–2104.

A. Plotkin
Associate Editor

Development of $\mathcal{O}(Nm^2)$ Preconditioned Multigrid Solvers for Euler and Navier–Stokes Equations

Jack R. Edwards*
North Carolina State University, Raleigh, North Carolina 27695
and
James L. Thomas†
NASA Langley Research Center, Hampton, Virginia 23681

Introduction

THE search for optimal convergence for Navier–Stokes calculations is turning toward a reexamination of implicit schemes based on approximate factorization, alternating-direction implicit (ADI), or relaxation techniques.[1–6] Newer procedures[3–6] utilize subiteration techniques to reduce factorization error, either globally[4–6] or locally,[3] as part of a planar relaxation procedure. Such techniques have also been implemented within an overall multigrid framework,[2,3,6] where they function as a powerful smoother for high- and medium-frequency error modes.

One such procedure[6] has been developed as an extension of the popular CFL3D code,[7] CFL3D-DDADI for the purposes of this work. In contrast to CFL3D, the implicit operator for CFL3D-DDADI is based on a diagonally dominant ADI factorization of the system Jacobian, including implicit formulations for the boundary conditions and the viscous terms. The diagonally dominant descriptor simply means that all diagonal elements of the Jacobian are retained in each tridiagonal factor.[4] This approximation, although better than conventional approximate factorization strategies, will still incur a Courant–Friedrichs–Lewy (CFL) restriction. In CFL3D-DDADI, this restriction is alleviated by a subiteration approach that drives the linear implicit residual toward a specified tolerance at each nonlinear iteration.[6]

Received 26 May 1999; presented as Paper 99-3263 at the AIAA 14th Computational Fluid Dynamics Conference, Norfolk, VA, 28 June–1 July 1999; accepted for publication 7 December 1999.

*Assistant Professor, Campus Box 7910, Department of Mechanical and Aerospace Engineering; jredward@eos.ncsu.edu. Senior Member AIAA.

†Head, Computational Modeling and Simulation Branch; j.l.thomas@larc.nasa.gov. Fellow AIAA.